

# 1 Size-differentiated Export in Different Dynamical 2 Regimes in the Ocean

3 **M. Dever<sup>1</sup>, D. Nicholson<sup>1</sup>, M. M. Omand<sup>2</sup>, and A. Mahadevan<sup>1</sup>**

4 <sup>1</sup>Woods Hole Oceanographic Institution, Woods Hole, MA 02543, USA

5 <sup>2</sup>Graduate School of Oceanography, University of Rhode Island, Narragansett, Rhode Island, USA

## 6 **Key Points:**

- 7 Submesoscale dynamics enhance the contribution of slow-sinking particles to  
8 POC export, depending on their intensity and on the fraction of biomass in the  
9 slow sinking particle classes.
- 10 Remineralization processes can enhance the contribution of slow-sinking parti-  
11 cles to the point where these particles sometimes dominate POC export

12      **Abstract**

13      Export of Particulate Organic Carbon (POC) is mainly driven by gravitational sinking.  
 14      Thus, traditionally, it is thought that larger, faster-sinking particles make up most of  
 15      the POC export flux. However, this need not be the case in a dynamic oceanic flow  
 16      field, where the ocean velocity can influence the descent rate of particles. Particles  
 17      with different settling speeds are released in two process-oriented model simulations  
 18      of an upper ocean eddying flow to evaluate the impact of (1) ocean dynamics on the  
 19      respective contribution of the different sinking-velocity classes to POC export, and  
 20      (2) the particle number size-spectrum slope. The analysis reveals that the leading  
 21      export mechanism changes from gravitationally-driven to advectively-driven as sub-  
 22      mesoscale dynamics become more important. The vertical velocity associated with  
 23      submesoscale dynamics enhances the contribution of slower-sinking particles to POC  
 24      export. A steeper particle size spectrum, also increases the relative contribution of  
 25      smaller, slower-sinking particles. Implementing a remineralization scheme generally  
 26      decreases the total amount of biomass exported, but its impact is weaker in dynamical  
 27      regimes where submesoscale dynamics are present and export is advectively-driven.  
 28      Under specific conditions, remineralization processes counter-intuitively enhance the  
 29      role of slower-sinking particles to the point where these slower-sinking velocity classes  
 30      dominate the export, therefore challenging the traditional paradigm for POC export.  
 31      This study demonstrates that slow-sinking particles can be a significant contribution,  
 32      and at times, even dominate the export flux.

33      **1 Introduction**

34      Photosynthesis in the sunlit upper ocean and the production of Particulate Or-  
 35      ganic Carbon (POC) takes up dissolved inorganic carbon and facilitates the uptake  
 36      of CO<sub>2</sub> from the atmosphere. The sinking of POC exports organic carbon from the  
 37      upper ocean to the interior, leading to the sequestration of carbon (Falkowski, Barber,  
 38      & Smetacek, 1998) on timescales ranging from days to years depending on the sink-  
 39      ing depth and circulation. Understanding the mechanisms driving the export of POC  
 40      from the ocean's surface to the interior is therefore crucial to better constrain Earth's  
 41      carbon budget.

42      Traditionally, POC export is thought to occur through gravitational sinking and  
 43      one-dimensional models have been used to describe the sinking POC flux with depth.  
 44      Particles produced through primary and secondary production in the surface layer  
 45      that are relatively large and fast-sinking, tend to sink out of the upper surface layer  
 46      on timescales shorter than the timescale on which the particles get remineralized.  
 47      It is reasonable to treat POC export as sinking-dominated if the vertical advective  
 48      velocities in the ocean are weaker than the velocities associated with gravitational  
 49      sinking. However, Particulate Organic Matter (POM) has a wide range of particle  
 50      shape, size and type, that result in particle sinking velocities ranging from practically  
 51      zero, to several hundreds of meters per day. The size spectrum, or number distribution  
 52      of particle sizes, is usually characterized by a power law with the power ranging between  
 53      -2 and -4, for which the abundance of small particles is  $\mathcal{O}(10^4 - 10^8)$  greater than large  
 54      particles. The biomass size spectrum, which indicates the distribution of biomass vs.  
 55      particle size, tends to be flatter and variable in shape (?) compared to the particle  
 56      number spectrum, because the volume (and mass) of a particle scales with its linear  
 57      size raised to a power that exceeds 1 (and typically varies between 2 and 3 depending on  
 58      shape and porosity). Importantly, it means that a significant fraction of the particulate  
 59      biomass is in the small size fraction. Even though the sinking velocity  $w_s$  of particles  
 60      does not perfectly relate to particle size  $l$ , it is fair to assume that  $w_s \sim l^n$  (with  
 61       $n = 2$  according to Stokes law, and  $1 < n < 2$  for complex particle shapes). Due to  
 62      this, as well as the fact that particles of organic matter are not very much greater in  
 63      their densities than seawater, a significant fraction of the biomass sinks very slowly (at

64 velocities less than tens of meters per day). When the gravitational sinking velocity  
 65 of particles is comparable to (or smaller than) the vertical velocities in the flow field,  
 66 the dynamics of the flow field can impact the trajectories and fate of the POC. Thus,  
 67 depending on the flow dynamics, and the fraction of slow-sinking particulate biomass,  
 68 the sinking of organic matter can be affected by the fluid flow in the ocean.

69 Recent studies have shown that ocean dynamics can play a role in driving the  
 70 transport of carbon from the euphotic layer to the ocean interior. For example, en-  
 71 hanced vertical velocities along the edge of a mesoscale eddy led to a funneling of par-  
 72 ticles along the eddy's periphery (van Haren, Millot, & Taupier-Letage, 2006; Waite  
 73 et al., 2016). Omand et al. (2015) found that submesoscale mixed layer eddies, while  
 74 contributing to the restratification of a frontal zone, were subducting a large amount  
 75 of non-sinking POC from the surface productive layer during the onset of the Spring  
 76 bloom in the subpolar North Atlantic. Advectively subducting plumes or filaments  
 77 of high oxygen, chlorophyll and small POC (evidenced through backscatter) were de-  
 78 tected from a suite of gliders during the North Atlantic Bloom experiment (?). Using  
 79 model simulations to capture the process of eddy-driven subduction, Omand et al.  
 80 (2015) estimated the downward advective flux of non-sinking POC and parameter-  
 81 ized it. ? quantified the flux of fast-sinking particles consisting largely of diatoms  
 82 from observations of optical backscatter. But, these estimates did not account for a  
 83 range of sinking particle velocities. Typically, particulate organic matter (POM) has a  
 84 wide spectrum of sinking velocities and in order to understand its fate and export, we  
 85 need to consider the biomass distribution as a function of the particle sinking velocity  
 86 spectrum and its interaction with the dynamics of the flow field in the ocean.

87 A growing body of literature focusing on submesoscale (1-10 km) dynamics is  
 88 exploring its impact on biogeochemical processes (Lévy, Ferrari, Franks, Martin, &  
 89 Rivière, 2012; Mahadevan, 2016). Submesoscale dynamics, characterized by Rossby  
 90 numbers of order 1, typically develop in filaments in areas where sharp density fronts  
 91 exist (Klein & Lapeyre, 2009; McWilliams, 2016; Thomas, Tandon, & Mahadevan,  
 92 2013). In this dynamical regime, geostrophic balance breaks down and a secondary  
 93 ageostrophic circulation develops across the front, capable of generating large vertical  
 94 velocities on the order of 100 m/day (Fox-Kemper, Ferrari, & Hallberg, 2008; Mahade-  
 95 van, 2016). On the denser side of the front, the vorticity is cyclonic and associated with  
 96 downwelling velocities, while anticyclonic vorticity and upwelling is expected on the  
 97 lighter side of the front. The distribution of relative vorticity across a front is asym-  
 98 metric and skewed toward cyclonic vorticity (Rudnick, 2001), leading to more localized  
 99 and more intense downwelling regions, as opposed to weaker and larger upwelling re-  
 100 gions (Mahadevan & Tandon, 2006). Enhanced vertical velocities can generate a local  
 101 bloom by supplying nutrients to the sunlit layer of the ocean (??), or can significantly  
 102 increase the export of POC to the ocean interior through downwelling (Estapa et al.,  
 103 2015; Lévy et al., 2012; Omand et al., 2015; ?).

104 The downwelling velocities  $\mathcal{O}(100 \text{ m/day})$  generated at submeso-scales provide  
 105 a physical mechanism capable of competing with gravitational sinking and thus ex-  
 106 porting particles over a larger portion of the particle size spectrum. Through this  
 107 mechanism, smaller particles can be exported on timescales shorter than their rem-  
 108 ineralization timescales, despite their slower sinking velocities. Depending on the frac-  
 109 tion of biomass in smaller particles (i.e., with slow sinking velocities), the impact of  
 110 submesoscale dynamics on the export of POC is potentially significant.

111 In this study, we account for a range of particle sinking velocities in a dynamic  
 112 flow field. Despite progress on sampling and viewing particles in the ocean (McDonnell  
 113 & Buesseler, 2010), direct measurements of particles sinking velocities are difficult  
 114 to obtain, and often inferred from key parameters such as particle type, size, and  
 115 density. Though we acknowledge a large variability in these relationships, we assume

116 a relationship between particle size, biomass, and particle sinking velocity in order to  
 117 assess the impact of the flow dynamics and particle size spectrum on the export flux.

118 We rely on a submesoscale-resolving, non-hydrostatic ocean model to simulate the  
 119 dynamics in the upper few hundred meters of the ocean. The model does not represent  
 120 surface waves or boundary layer turbulence, but rather, examines the fate of particulate  
 121 organic matter beneath the turbulent surface boundary layer. The dynamical model  
 122 is coupled with a particle-tracking module to model the advection of particles by fluid  
 123 flow, while neglecting the effects of particle inertia and drag on their advection. In  
 124 addition, the particles sink with a range of sinking velocities (between 0.025–5 m  
 125 day<sup>-1</sup>).

126 The model is used to quantify the contribution of slow-sinking particles to carbon  
 127 export, as a function of (1) the dynamics of the flow field, (2) the slope of the sinking  
 128 velocity spectrum, and (3) the remineralization timescale. Particles in the model  
 129 are prescribed with both a constant and time-varying sinking velocity to mimic a  
 130 remineralizing behavior. Particles are released in two fundamentally different flow  
 131 fields in terms of dynamics based on observed conditions in the Northeast Pacific:  
 132 In the summer, where ocean dynamics are characterized by low Rossby numbers and  
 133 weak vertical advective velocities, and in the winter, where ocean dynamics include  
 134 submesoscale frontal structures and local Rossby numbers  $\mathcal{O}(1)$ . Both simulations  
 135 and the particle-tracking module are described in Section 2. The impact of particles  
 136 characteristics and ocean dynamics on the export of POC is quantified in Section 3,  
 137 and discussed in Section 4. Section 5 summarizes the key conclusions of the study.

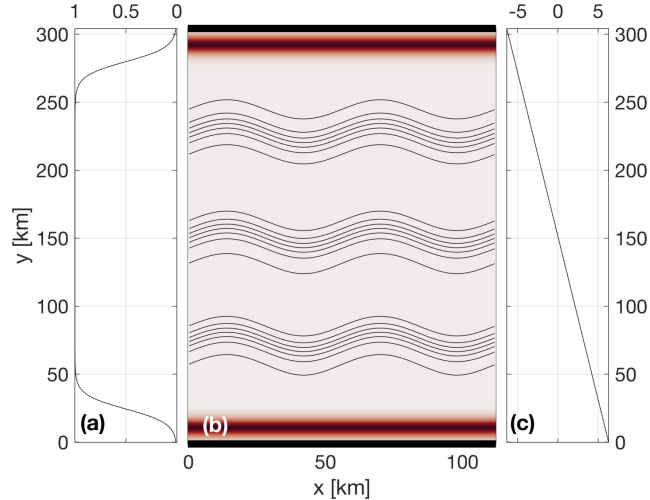
## 138 2 Methods

### 139 2.1 Model setup and domain

140 This study uses a non-hydrostatic, three-dimensional, Process Study Ocean Model  
 141 (PSOM; Mahadevan, Oliger, & Street, 1996a, 1996b) to simulate an eddy field that is  
 142 representative of the Northeast Pacific Ocean. The model is set in a channel configura-  
 143 tion with periodic east-west boundaries, and solid boundaries in the south and north.  
 144 The domain covers 112 km in the x-direction, 304 km in the y-direction, and 1000 m  
 145 in the vertical (Figure 1). The horizontal resolution is 500 m, while a stretched grid is  
 146 used in the vertical with 32 levels ranging in thickness from 1.25 m near the surface to  
 147 70 m at the lowermost level. The model is integrated numerically in time and evolves  
 148 the temperature, salinity, free-surface height, pressure, and three-dimensional velocity  
 149 field from an initial state, subject to momentum and buoyancy fluxes applied through  
 150 the surface boundary.

158 Time-varying wind stress and heat flux are prescribed at the surface boundary.  
 159 Time series are computed from measurements collected at Station Papa and available  
 160 through the Pacific Marine Environmental Laboratory (?). Daily wind stress and net  
 161 heat fluxes are calculated over the period 2007–2016 to produce a year-long climatology.  
 162 A squared low-pass filter with a cut-off frequency of 8.5 days is applied to both time  
 163 series to remove high-frequency variability. In all numerical experiments, simulations  
 164 are run for the first 5 days without any forcing applied to the surface boundary. Surface  
 165 wind stress and heat fluxes are then linearly ramped up between days 5 and 10 of the  
 166 simulation, to reach realistic values at day 10.

167 While the meridional component,  $\tau_y$ , is set to zero, the zonal component of  
 168 the wind stress,  $\tau_x$ , is prescribed at the surface throughout the model domain and  
 169 is tapered at the northern and southern boundaries to avoid excessive Ekman-driven  
 170 upwelling and downwelling (Figure 1a). A restoration timescale is prescribed to contain  
 171 the curl-driven upwelling and downwelling regions generated by the tapering of the  
 172 wind stress, as well as to limit internal wave reflection at the solid boundaries back



151 **Figure 1.** PSOM model setup. (a) Meridional profile of scaling coefficient that multiplies the  
 152 time-varying zonal wind stress  $\tau_x$  shown in Fig. 3a. The taper at north and south boundaries  
 153 prevents ‘coastal’ up-/down-welling being entirely concentrated in the boundary grid cell. (b)  
 154 Restoration factor (color shading) used to dampen internal wave reflection at boundaries as well  
 155 as up-/down-welling due to the windstress curl. Surface density contours (black) show the three  
 156 fronts used to initialize the model. (c) Meridional variation of the time-dependent surface heat  
 157 flux (Fig. 3a) prescribed over the domain.

173 into the domain (Figure 1b). While net surface heat fluxes are homogeneous in the  
 174 zonal direction, a meridional gradient is maintained throughout the simulation. The  
 175 meridional gradient was determined from the North American Regional Reanalysis  
 176 (NARR) product (Mesinger et al., 2006), and set to  $1/24 \text{ W/m}^2/\text{km}$  (Figure 1c).

177 Initial hydrographic conditions are determined from a three-dimensional grid-  
 178 ded field of temperature and salinity from Argo floats (Gaillard, Reynaud, Thierry,  
 179 Kolodziejczyk, & von Schuckmann, 2016; ?). Argo data is averaged monthly over the  
 180 period 2002-2012 and two different months are used to initialize the two main numerical  
 181 experiments for this study: Climatological conditions in April are used to initialize  
 182 the *Papa-summer* experiment, while January climatological conditions are used to ini-  
 183 tialize the *Papa-winter* experiment (Table 1). The north-south background density  
 184 gradient is then intensified into three fronts located at  $y = 75$ ,  $y = 150$ , and  $y = 225$   
 185 km (Figure 1). The amplitude of the density gradient associated with the three fronts  
 186 is determined from the probability distribution function (PDF) of the density gradients  
 187 measured by underwater gliders deployed around Station Papa over the period 2008-  
 188 2010 (Pelland, Eriksen, & Cronin, 2016; ?). To reduce model spin-up time, density  
 189 fronts are perturbed by a sinusoidal wave with a wavelength close to the 1st baroclinic  
 190 deformation radius ( $\lambda = 66 \text{ km}$ ). Similar PSOM configurations were successfully used  
 191 in previous studies (Mahadevan, D’Asaro, Lee, & Perry, 2012; Omand et al., 2015).

192 Two main experiments are conducted using the same configuration of PSOM,  
 193 where only initial conditions and surface forcings are varied: *Papa-summer* aims  
 194 at generating ocean dynamics representing conditions in the Northeast Pacific in  
 195 the summertime. Summer ocean dynamics are characterized by a flow generally in  
 196 geostrophic balance, with relatively weak density gradients and low Rossby numbers  
 197 ( $\ll 1$ ). *Papa-winter* aims at capturing wintertime ocean conditions in the region. A  
 198 different dynamical regime is expected to dominate during wintertime when mixed

217 **Table 1.** Summary of the key characteristics of PSOM experiments *Papa-summer* and  
 218 *Papa-winter*.

	<i>Papa-summer</i>	<i>Papa-winter</i>
Time period	April – July	January – March
Spin-up	60 days	50 days
Advective timestep	216 s	108 s
Horizontal diffusivity	$1 \text{ m}^2 \text{ s}^{-1}$	$0.2 \text{ m}^2 \text{ s}^{-1}$
Restoration timescale	3 days	15 days
Zonal wind stress	$0 - +0.16 \text{ N m}^{-2}$	$-0.05 - +0.17 \text{ N m}^{-2}$
Surface heat flux	$-46.8 - +167.5 \text{ W m}^{-2}$	$-57.6 - +15.3 \text{ W m}^{-2}$
Maximum $M^2 (\times 10^{-8})_{\text{initial spun-up}}$	$12.0 \text{ s}^{-2}$	$33.9 \text{ s}^{-2}$
Maximum $N^2 (\times 10^{-4})_{\text{initial spun-up}}$	$3.1 \text{ s}^{-2}$	$1.6 \text{ s}^{-2}$
Averaged mixed layer depth $_{\text{initial spun-up}}$	73 m	85 m

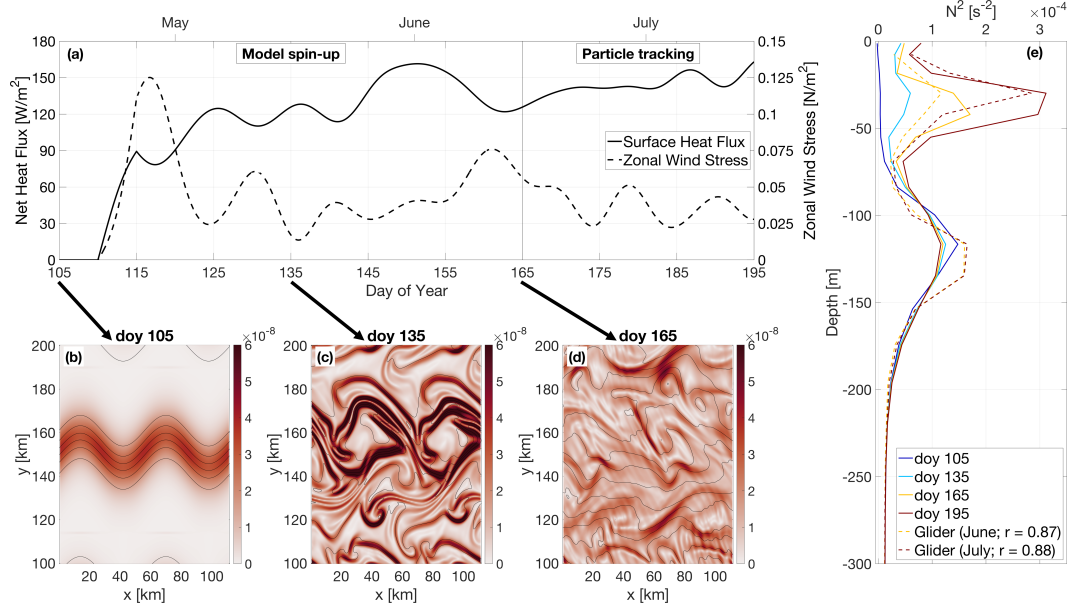
199 layers are deeper and lateral density gradients enhanced, with sharper density fronts,  
 200 filament-like features and localized Rossby number  $\mathcal{O}(1)$  over spatial scales  $\mathcal{O}(1 \text{ km})$   
 201 (Callies, Ferrari, Klymak, & Gula, 2015; Mensa et al., 2013; Thompson et al., 2016).  
 202 The individual characteristics of each of  
 203 *Papa-summer* and *Papa-winter* are detailed below.

### 204 2.1.1 *Papa-summer* Model Experiment

205 In *Papa-summer*, PSOM is initialized based on climatological Argo data in April.  
 206 The magnitude of the density gradient across the front is set to  $3.34 \times 10^{-6} \text{ kg/m}^3/\text{m}$ ,  
 207 which corresponds to the 95<sup>th</sup> percentile of the PDF of density gradients measured  
 208 in April from glider data collected in the region (Figure 2 and Table 1). The model  
 209 is run with a timestep of 216 s and is allowed to spin-up for 60 days, allowing sum-  
 210 mer stratification to develop. The model is then run for 30 additional days, saving  
 211 instantaneous model fields every 3 hours for particle tracking. The month of April  
 212 is chosen for initialization so the experiment would capture the onset of positive net  
 213 heat fluxes, and the summer restratification that ensues in July-August (Figure 2). In  
 214 this region, the summer stratification is associated with large primary productivity,  
 215 particle production, and POC export (e.g., fecal pellets, dead phytoplankton; Plant  
 216 et al., 2016).

### 228 2.1.2 *Papa-winter* Model Experiment

229 In *Papa-winter*, PSOM is initialized based on climatological Argo data in Jan-  
 230 uary. The frontal gradient is set to  $3.54 \times 10^{-5} \text{ kg/m}^3/\text{m}$ , which corresponds to the  
 231 99<sup>th</sup> percentile of the PDF of density gradients measured in January from glider data  
 232 collected in the region (Figure 3 and Table 1). The model is allowed to spin-up for 50  
 233 days allowing for the prescribed fronts to become unstable. To accommodate for the  
 234 larger density gradients and stronger velocities, the advective timestep is shortened to  
 235 108 s and the horizontal diffusivity is lowered to  $0.2 \text{ m}^2/\text{s}$  throughout the experiment.  
 236 The model is run for 30 additional days, saving instantaneous model fields every 1.5  
 237 hours for particle tracking. The month of January is chosen for initialization so the  
 238 experiment would capture the time of year where the mixed layer is the deepest, and  
 239 Rossby number  $\mathcal{O}(1)$  occur more frequently. The objective is for this experiment to



219 **Figure 2.** PSOM configuration for *Papa\_summer*. (a) Time series of net heat fluxes and wind  
 220 stress prescribed at the surface. Notice the positive heat fluxes, as well as downfront winds (i.e.  
 221 eastward) persisting throughout the experiment. (b)-(d) surface horizontal buoyancy gradients  
 222  $M^2 = |\nabla_H b|^2$  (in  $\text{s}^{-2}$ ) at day of year (doy) 105, 135, and 165. Black contours show isopycnals (in  
 223  $\text{kg}/\text{m}^3$ ; CI = 0.01  $\text{kg}/\text{m}^3$ ). (e) Vertical profile of the buoyancy frequency  $N^2$  at day of year 105,  
 224 135, 165, and 195, showing the development of summer stratification centered at  $z = 30 \text{ m}$  (solid  
 225 lines). Monthly-average vertical stratification obtained from glider profiles collected in June and  
 226 July are superimposed (dashed lines), along with the correlation coefficient between observations  
 227 and model outputs.

240 contrast *Papa\_summer* by capturing the statistics of ocean conditions dominated by  
 241 submesoscale dynamics.

### 250 2.1.3 Validation

251 To ensure that PSOM simulations yielded realistic conditions for both *Papa\_summer*  
 252 and *Papa\_winter*, distributions of horizontal ( $M^2$ ) and vertical ( $N^2$ ) buoyancy gradi-  
 253 ents are compared with glider observations collected over the period 2008-2009 (Pelland  
 254 et al., 2016). During this period, underwater gliders sampled in a “bow-tie” pattern  
 255 centered on Station Papa. Gliders sample the water column in a triangular wave  
 256 pattern, whose shape is easily affected by currents, due to the slow moving speed of  
 257 the glider (~1 km/hr). It is therefore challenging to associate a specific spatial scale  
 258 with gradients computed between glider profiles, as profile separation distances can be  
 259 highly variable through depth and time. To circumvent this issue, horizontal buoy-  
 260 ancy gradients are computed between each pair of glider profiles available within one  
 261 branch of the bow-tie. Each along-track lateral buoyancy gradient is thus associated  
 262 with a specific separation scale and a timestamp. Glider-based density gradients can  
 263 be affected by internal waves. To filter the impact of internal waves on the PDF of  
 264 horizontal buoyancy gradients, only gradients computed at a scale of twice the Rossby  
 265 radius  $\pm 1 \text{ km}$  are considered. Rossby radii are estimated from the glider data and  
 266 are  $\sim 8 \text{ km}$  in winter and  $\sim 20 \text{ km}$  in summer.

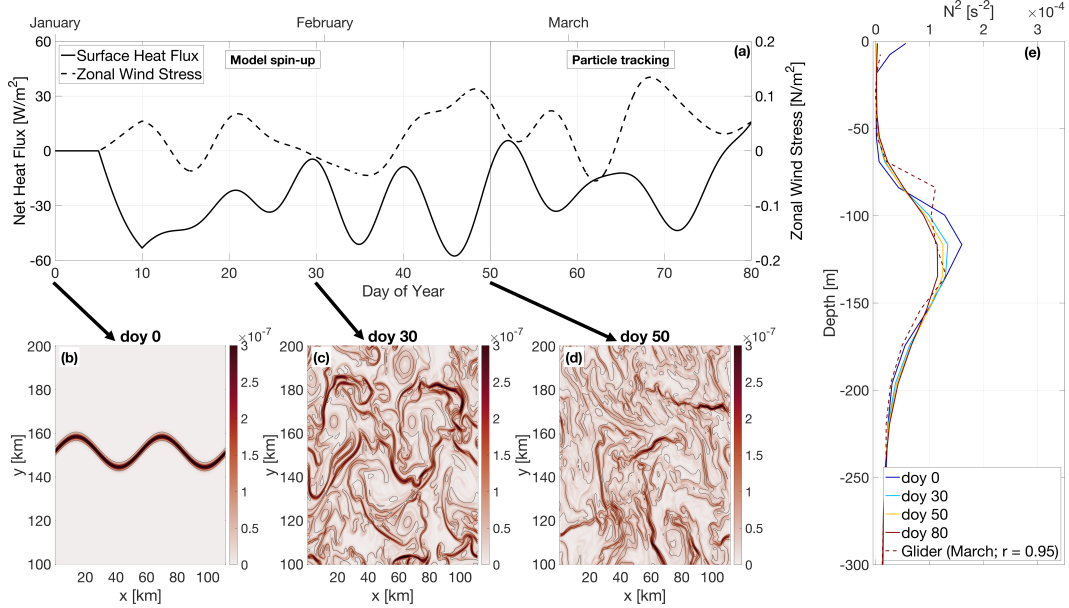


**Figure 3.** PSOM configuration for *Papa\_winter*. (a) time series of net heat fluxes and wind stress prescribed at the surface. Notice the mostly negative heat fluxes, as well as alternating zonal wind direction. (b)-(d) surface horizontal buoyancy gradients  $M^2 = |\nabla_H b|^2$  (in  $s^{-2}$ ) at day of year (doy) 0, 30, and 50. Black contours show isopycnals (in  $kg/m^3$ ; CI = 0.01  $kg/m^3$ ). (e) Vertical profile of the buoyancy frequency  $N^2$  at doy 0, 30, 50, and 80, showing the persistence of the halocline between  $z = 80$  and  $z = 180$  m throughout the experiment (solid lines). Monthly-average vertical stratification obtained from glider profiles collected in March is superimposed (dashed line), along with the correlation coefficient between observations and model outputs.

## 2.2 Particle Tracking Experiments

### 2.2.1 Particle Advection Scheme

To quantify the impact of submesoscale dynamics on the export of Particulate Organic Matter (POC), Lagrangian particle trajectories are computed using the same scheme as in “TRACMASS” (Döös, Kjellsson, & Jönsson, 2013) with the flow fields from the two experiments described above. The three-dimensional, non-divergent velocity components from the faces of each “C” grid cell are linearly interpolated onto the particle’s position within the grid cell. For example, the eastward (along the x-axis) velocity of a particle is given by

$$u(x) = u_{i-1} + \frac{(x - x_{i-1})}{(x_i - x_{i-1})}(u_i - u_{i-1}), \quad (1)$$

where the subscripts  $i - 1$  and  $i$  denote the western and eastern walls of the grid cell where the particle is located, respectively. This can be re-written as

$$\frac{\partial x}{\partial t} + \beta x + \delta = 0, \quad (2)$$

where  $\beta = (u_i - u_{i-1})/\Delta x$  and  $\delta = -u_{i-1} - \beta x_{i-1}$  (Döös et al., 2013). This differential equation can be solved analytically for  $\beta \neq 0$  as

$$x_{t_1} = \left( x_0 + \frac{\delta}{\beta} \right) \exp^{-\beta(t_1 - t_0)} - \frac{\delta}{\beta} \quad (3)$$

280 The time it will take for the particle to reach the eastern or western face of the grid  
 281 cell can be computed by taking  $x_{t_1} = x_i$  or  $x_{t_1} = x_{i-1}$ , respectively, and solving for  
 282  $t_1$ . For each advective timestep, the times required for the particle to reach any of the  
 283 6 walls of the grid cell are computed using (3). If any of those times is shorter than  
 284 the advective timestep, the particle is advected until it reaches the cell wall. Then the  
 285 flow field in the adjacent grid cell is considered and the particle is advected over the  
 286 remaining time.

### 287 2.2.2 Particle Seeding

288 For all particle-tracking experiments, a single particle seeding event is prescribed.  
 289 In the horizontal, particles are seeded every 250 m over the entire domain in the x-  
 290 direction, and for  $100 < y < 200$  km in the y-direction. The seeding is centered over  
 291 the mean position of the central front (see Figure 2) and is therefore not affected by  
 292 undesired effects created by the solid north-south solid boundaries. In the vertical,  
 293 particles are seeded every 1 m between 75 and 85 m. This depth range is chosen as it  
 294 corresponds to the average euphotic depth at Station Papa, defined by the 1% light  
 295 level. The euphotic depth was computed for the months of February and June over  
 296 the period 2007-2016 from profiles of Photosynthetically Available Radiation (PAR)  
 297 collected at Station Papa as part of the long-term monitoring of Line P executed by the  
 298 Department of Fisheries and Ocean Canada<sup>1</sup>. The average euphotic depth computed  
 299 for both of these months is around 80 m, which agrees with previously established  
 300 estimates of the euphotic depth (Harrison, Whitney, Tsuda, Saito, & Tadokoro, 2004;  
 301 Sherry, Boyd, Sugimoto, & Harrison, 1999).

302 In each particle-tracking experiment, four different classes of particles are re-  
 303 leased. Each particle class is characterized by a different sinking velocity: 0.025, 0.05,  
 304 1, and 5 m/day. The slowest-sinking class is essentially selected to represent non-  
 305 sinking particles: based on the setup of our experiments, the slowest-sinking particles  
 306 would take 800 days on average to be exported to a depth of 100 m through gravi-  
 307 tational sinking, a timescale much greater than commonly observed remineralization  
 308 timescales. The fastest-sinking velocity is chosen as an end-member velocity class of  
 309 particle that will be exported in its entirety over the course of our experiment.

310 The advective timestep for particles is set to 1.5 hours. The flow field is linearly  
 311 interpolated in time between model outputs, justifying the higher temporal resolution  
 312 used for particle tracking in *Papa\_winter*. Particle positions are saved every 3 hours,  
 313 along with key model variables interpolated onto the particle positions (e.g., density,  
 314 vorticity). Particles are tracked for three weeks (28 days). Each particle-tracking ex-  
 315 periment contains 1,971,717 particles per sinking-velocity class, for a total of 9,858,585  
 316 particles. Particles located deeper than the maximum winter mixed layer (i.e., 100 m;  
 317 Pelland et al., 2016; Plant et al., 2016) are considered exported, as they will likely not  
 318 be re-entrained into the mixed layer.

### 319 2.2.3 Density and Biomass Spectra

320 The slope  $\xi$  of the size spectrum of particles (also known as the Junge slope; White  
 321 et al., 2015) is the slope of the log-log curve of particle number  $N$  vs. particle radius  
 322  $r$ , where

$$N(r) = N_0 \left( \frac{r}{r_0} \right)^{-\xi}. \quad (4)$$

323 Here,  $N_0$  and  $r_0$  represent a reference particle number and radius, chosen arbitrarily.  
 324 For small particles ( $<400$   $\mu\text{m}$ ) and relatively low temperature ( $<15^\circ\text{C}$ ), it has been

---

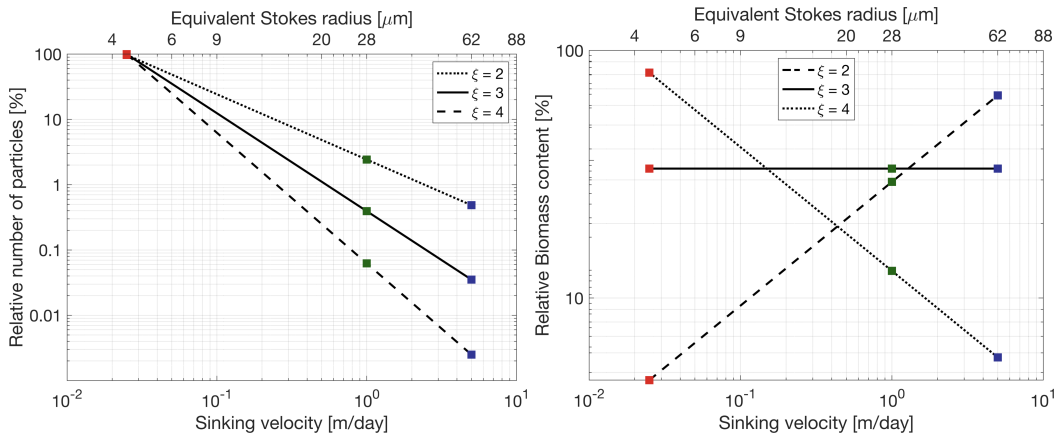
<sup>1</sup> <https://www.waterproperties.ca/linep/index.php>

325 shown that the relationship between particle radius  $r$  and sinking velocity  $w_s$  exhibits  
 326 a range of variation and is difficult to determine empirically. Nevertheless, Stokes' law,  
 327 where  $w_s \propto r^2$ , is often used as a lower-bound sinking velocity estimate (Bach et al.,  
 328 2012).

329 Assuming a Stokes-like relationship, we can construct a particle sinking velocity  
 330 spectrum  $N(w_s)$  based on (4), as

$$N(w_s) = N_0 \left( \frac{w_s}{w_{s_0}} \right)^{-\xi/2}, \quad (5)$$

335 where  $w_{s_0}$  is the sinking speed of particles with radius  $r_0$ . For a specific slope and  
 336 sinking-velocity class, an equivalent number of particles per simulated particle can be  
 337 computed using (5) (See Figure 4). For example, using the largest sinking velocity  
 338 class as a reference (i.e.,  $w_{s_0} = 5$  m/day and  $N_0 = 1,971,717$ ), and a spectral slope  
 339  $\xi = 4$ , each simulated particle with a sinking velocity of 0.025 m/day in fact represents  
 340 40,000 particles (Figure 4). The relative biomass of a particle in a specific sinking-  
 341 velocity class,  $B_p(w_s)$  can be estimated if the biomass is assumed to scale with the  
 342 particle's volume. The relative biomass of one particle in a sinking-velocity class  $w_s$   
 can therefore be computed as



331 **Figure 4.** Relative number of particles (left) and biomass (right) as a function of sinking  
 332 velocity  $w_s$ . Sinking velocity spectrum are shown for three different Junge slope  $\xi$ : 2 (dotted),  
 333 3 (solid), and 2 (dashed). Colored squares indicate the sinking velocities of the three particle  
 334 classes modeled: 0.025 m/day (red), 1 m/day (green), and 5 m/day (blue).

$$B_p(w_s) = B_p(w_{s_0}) \left( \frac{w_s}{w_{s_0}} \right)^{3/2} \quad (6)$$

344 where  $B_p(w_{s_0})$  is the biomass of a particle in the sinking velocity class  $w_{s_0}$ . The total  
 345 biomass associated with one simulated particle can be obtained by scaling (6) by the  
 346 ratio  $N(w_s)/N_0$ :

$$B(w_s) = B_0 \left( \frac{w_s}{w_{s_0}} \right)^{3/2} \frac{N(w_s)}{N_0} \quad (7)$$

347 where  $B_0 = B_p(w_{s_0})$ . Combining (5) and (7) yields an expression relating the biomass  
 348 associated with a simulated particle for a specific sinking-velocity class and the spectral  
 349 slope (Figure 4):

$$B(w_s) = B_0 \left( \frac{w_s}{w_{s_0}} \right)^{\frac{3-\xi}{2}}. \quad (8)$$

Using the same example as before where  $\xi = 4$ , if the amount of biomass associated with one simulated particle in the 5 m/day sinking-velocity class is taken as  $B_0 = 1$ , then one simulated particle sinking at 0.025 m/day contains 14.14 units of biomass and a single particle contains  $14.14/40,000 = 3.5 \times 10^{-4}$  units of biomass (see Figure 4). This normalized formulation of particle number and biomass (see Equations (5) and (8)) has the advantage that the impact of spectral slope on the relative export of biomass can be quantified without needing a large number of particle-tracking experiments, where the number of seeded particles would vary to account for the different spectral slopes. For the purpose of this study, only the relative amount of biomass is relevant. For simplicity, we define a normalized biomass unit for  $\xi = 3$  as  $B_0 = 1$ . The values taken by  $B_0$  for other Junge slopes  $\xi$  are computed under the condition that the total amount of biomass is kept constant (Figure 4b).

### 2.2.4 Particle Remineralization Scheme

Remineralization of particles as they sink through the water column impacts the amount of biomass exported. Slow-sinking particles generally contain less biomass and spend more time in the mixed layer, which means that they are remineralized at a shallower depth than faster sinking particles. Remineralization processes are complex, species-dependent, and generally not well-understood. In the absence of a consensus on a general functional form of particle remineralization, we rely on an idealized relationship which assumes that the biomass content of a particle decreases in time proportionally to the particle volume. Remineralization is thus modeled as an exponential decrease of biomass with time at a rate  $k$  (Iversen & Ploug, 2010, 2013)

$$B(t) = B^0 \exp(-kt), \quad (9)$$

where  $B^0$  denotes the biomass content at  $t = 0$  days, and the remineralization rate is taken to be  $k = 0.13 \text{ day}^{-1}$  in this study (Iversen & Ploug, 2010). This remineralization rate is independent of particle sinking velocity, and seems to lie within the range of other estimates (Iversen & Ploug, 2010, 2013; Ploug, Iversen, Koski, & Buitenhuis, 2008). The change in biomass with time is in turn expected to affect the sinking velocity of the particle. Given that  $B \propto w^{3/2}$  (see Equation (6)), particles in all sinking-velocity classes undergo a decay in sinking speed according to

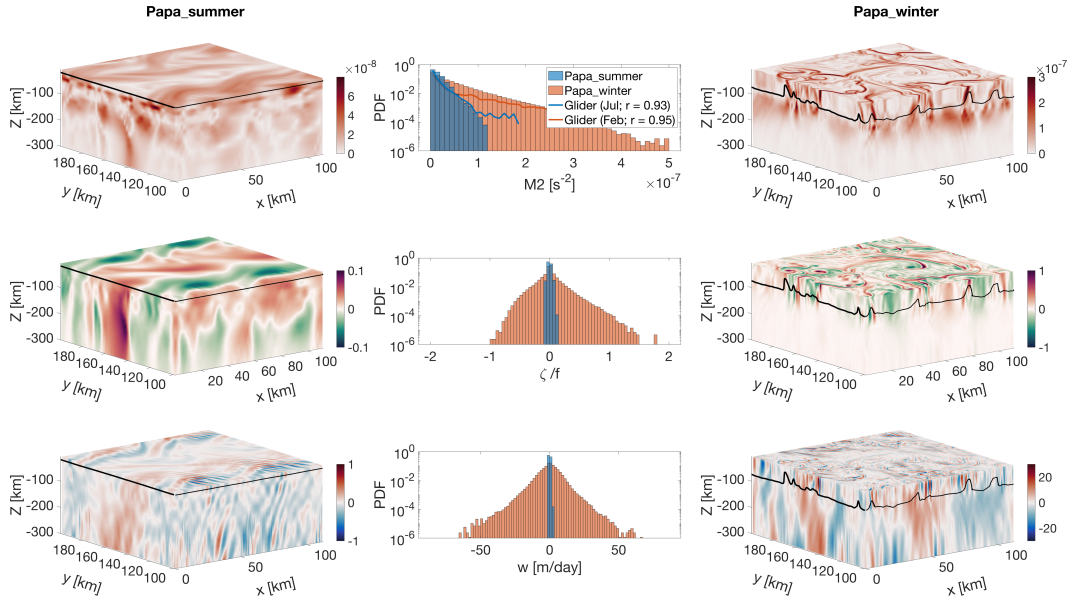
$$w_s(t) = w_s^0 \exp\left(-\frac{2kt}{3}\right), \quad (10)$$

where  $w_s^0$  is the initial sinking velocity at  $t = 0$  days. In this study, the impact of remineralization is thus considered through the implementation of a time-dependent sinking velocity (Equation 10). While particles classes are classified based on their initial sinking-velocity, it is worth noting that over the length of the particle-tracking experiments that include remineralization (28 days), particle sinking speeds slow down to 10% of their initial velocity.

## 3 Results

### 3.1 Seasonally varying dynamical regimes

Two model experiments are designed to capture different dynamical conditions observed in the Northeast Pacific Ocean in summer and winter. *Papa\_summer* is initialized in early spring (doy 105) when the water column is characterized by a relatively deep mixed layer ( $\sim 100$  m) and a halocline located between 100 and 150 m (Figure 2). The forcing by a realistic, positive, net heat flux generates the restratification of the water column, with the development of a strong thermocline between 25 and 50 m leading to the shoaling of the mixed layer and a subsurface peak in  $N^2$  at about 30 m (see Figure 2). A comparison between model outputs and monthly-averaged density



409 **Figure 5.** Snapshots of  $M^2$  (top),  $\zeta/f$  (middle), and  $w$  (bottom) half-way through the  
 410 particle tracking experiment for *Papa\_summer* (left) and *Papa\_winter* (right), with the Mixed Layer  
 411 Depth indicated by the solid black line. The corresponding Probability Distribution Functions  
 412 (PDFs) are shown in the center for both *Papa\_summer* (blue) and *Papa\_winter* (red). Note the  
 413 different colorbars used for *Papa\_summer* and *Papa\_winter*. Histograms of  $M^2$  computed from  
 414 glider data at Station Papa in February (blue line) and July (red line) are superimposed in the  
 415 top middle panel.

395 profiles from underwater gliders collected in June and July over the period 2008–2009  
 396 yields correlation coefficients of  $r = 0.87$  and  $r = 0.88$ , respectively. These high cor-  
 397 relation suggest that *Papa\_summer* numerical experiment captures the vertical spring  
 398 and summer conditions in the Northeast Pacific Ocean.

399 In the horizontal, the prescribed density fronts progressively become unstable  
 400 within the first 60 days of the experiment (Figure 2). During this time, the Total  
 401 Kinetic Energy (KEtot) contained in the model domain slowly increases before reach-  
 402 ing a maximum at doy 162, where it remains relatively constant for the rest of the  
 403 simulation. The flattening of the KEtot curve is used to determine the time necessary  
 404 for the simulation to spin-up, hence determining the start day of the particle-tracking  
 405 experiments. The ocean dynamics associated with *Papa\_summer* are characterized  
 406 using PDFs of horizontal buoyancy gradients ( $M^2 = |\nabla_H b|^2$ ), vertical velocities ( $w$ ),  
 407 and Rossby numbers computed from the normalized vertical component of the relative  
 408 vorticity ( $\text{Ro} = (v_x - u_y)/f$  where  $f = 1.12 \times 10^{-4}$ ; Figure 5).

416 Lateral buoyancy gradients in the summer are relatively weak  $\mathcal{O}(10^{-8} \text{ s}^{-2})$  and  
 417 result in low Rossby numbers  $\mathcal{O}(0.1)$ , with positive relative vorticity on the denser  
 418 (north) side of the front and negative relative vorticity on the lighter (south) side  
 419 of the front. Corresponding vertical velocities are consistently weaker than 1 m/day  
 420 ( $< 10^{-5} \text{ m/s}$ ) and are characterized by regions of weak upwelling and downwelling on  
 421 10 km scales, associated with the meandering of the front (Bower & Rossby, 1989).  
 422 Alternating bands of upwelling and downwelling at  $\mathcal{O}(1 \text{ km})$  spatial scale are super-  
 423 imposed, and likely caused by propagating internal waves. Coherent vertical velocities  
 424 structures extend to depths much greater than the mixed layer depth ( $\sim 25 \text{ m}$ ; Figure

425 5). The amplitude of the vertical velocity field coincides with the expected order of  
 426 magnitude given by the scaling  $w \propto Ro f U / N$  (Mahadevan, 2016): using  $Ro \sim 0.1$   
 427 (Figure 5),  $N \sim 10^{-2} \text{ s}^{-1}$  (Figure 2),  $f \sim 10^{-5} \text{ s}^{-1}$ , and  $U \sim 0.01 \text{ m/s}$ , we obtain  
 428  $w \sim 10^{-6} \text{ m/s}$ , or  $\sim 10^{-1} \text{ m/day}$ .

429 *Papa-winter* is, on the other hand, initialized in the winter (doy 0) to capture a time period where the mixed layer depth is deeper ( $\sim 100 \text{ m}$ ) and density gradients more pronounced (Pelland et al., 2016). At this time of year, the water column in this region is characterized by the presence of a deep halocline between 100 and 150 m (Figure 3 Pelland et al., 2016). After spin-up, the vertical stratification remains consistent throughout the model run, and compares well with the vertical profile obtained from glider observations for the month of March ( $r = 0.95$ ; see Figure 3). In the horizontal, prescribed density fronts are much sharper than in summer (i.e., over smaller spatial scales  $O(1 \text{ km})$  vs.  $O(10 \text{ km})$ ). Because of these stronger density gradients, combined with the alternating zonal winds and constantly negative surface heat flux, the fronts become unstable more rapidly than in summer (Figure 3). As a result, KEtot starts to plateau at doy 48. The experiment is considered spun-up by doy 50 and the particle-tracking experiment is initialized.

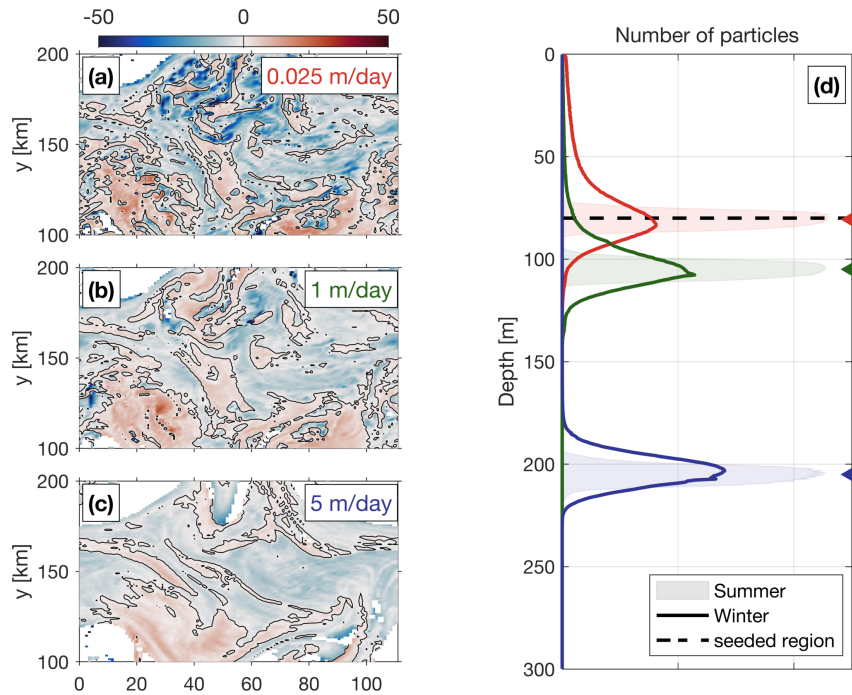
442 The frontal structures visible in the horizontal buoyancy gradient field are associated with filaments of relatively high Rossby number of  $\mathcal{O}(1)$  (Figure 5). The  
 443 PDF of relative vorticity reveals a positively-skewed distribution ( $s = 0.68$ ). This is in  
 444 agreement with the fact that the relative vorticity is more likely to be cyclonic than anticyclonic,  
 445 based on conservation of potential vorticity (Hoskins & Bretherton, 1972). Regions with high Rossby number are localized and located in the mixed layer exclusively.  
 446 In places where the local Rossby number reaches  $\mathcal{O}(1)$ , geostrophic balance is lost and a vertical secondary ageostrophic circulation begins to slump the isopycnals  
 447 and restore the flow to a more geostrophically-balanced flow. This ageostrophic secondary  
 448 circulation therefore generates “hot spots” of higher vertical velocities. The fine-scale structures in the vertical velocity field corresponding to  $\mathcal{O}(1)$  Rossby numbers  
 449 can be seen in Figure 5, with local vertical velocities up to 60 m/day ( $\sim 7 \times 10^{-4}$   
 450 m/s). Contrary to the PDF of relative vorticity, the distribution of vertical velocities  
 451 demonstrate a negative skewness ( $s = -0.25$ ). This is in agreement with the theory:  
 452 In fact, positive relative vorticity is associated with the dense side of a density front,  
 453 where vertical velocities are negative (Mahadevan, 2016). Once again, the amplitude  
 454 of these vertical velocity hot spots is coherent with the scaling  $w \propto Ro f U / N$ : using  
 455  $Ro \sim 1$ ,  $N \sim 10^{-2} \text{ 1/s}$ ,  $f \sim 10^{-5} \text{ 1/s}$ , and  $U \sim 0.1 \text{ m/s}$ , we obtain  $w \sim 10^{-4} \text{ m/s}$ , or  
 456  $\sim 10^1 \text{ m/day}$ .

461 Comparing *Papa-summer* and *Papa-winter* highlights the different dynamical  
 462 regimes in the two experiments. In *Papa-winter*, density fronts tend to be sharper,  
 463 meaning larger density gradients over shorter spatial scales. When computed at the  
 464 kilometer-scale, the PDF of horizontal buoyancy gradients in *Papa-winter* exhibits a  
 465 longer tail than in *Papa-summer* (Figure 5). When compared to observations, the  
 466 PDFs of  $M^2$  in *Papa-summer* and *Papa-winter* demonstrate a correlation with obser-  
 467 vations of  $r = 0.93$  and  $r = 0.95$ , respectively.

468 The wider PDF of vertical velocities in *Papa-winter* shows advective velocities  
 469 that match and exceed typical gravitational sinking velocities, particularly for smaller,  
 470 and therefore slower-sinking, particulate organic material. The secondary ageostrophic  
 471 circulation that develops at submeso-scales (i.e.,  $Ro \mathcal{O}(1)$ ) therefore generates an ex-  
 472 port mechanism that directly competes with the traditional paradigm that relies on  
 473 gravitational sinking leading the export of particulate matter in the ocean.

### 474 3.2 Gravitational and Advective Export of POC

475 Both model experiments described above were then used to investigate the re-  
 476 lationship between ocean dynamics and particle downward flux, using Lagrangian  
 477 particle-tracking. Domain-averaged, downward particle flux is expected to be a com-  
 478 bination of the flux driving by gravitational sinking ( $\langle w_s B \rangle$ ), and by the vertical ad-  
 479 vective currents affecting the particle along its pathway ( $\langle wB \rangle$ ). The deviation in  
 480 particle depths from the traditional one-dimensional gravitationally driven model is  
 481 shown in Figure 6 for both summer and winter cases. In the summer, the PDF of par-  
 482 ticle density versus depth remains relatively narrow through time, and is centered on  
 483 a depth level that can be predicted using a simple 1D gravitational model (see shaded  
 484 curves in Figure 6). The spread in the particle density also vary little among particle  
 485 classes with different sinking velocities, suggesting that downward fluxes of particles  
 486 is greatly dominated by gravitational settling and is not subject to significant vertical  
 487 ocean currents.



488 **Figure 6.** [left] The median depth anomaly of particles with a sinking speed (a) 0.025 m/d,  
 489 (b) 1 m/d, (c) 5 m/d within each grid cell for the winter case 25 days after particles are released.  
 490 The ‘depth anomaly’ is with respect to the ‘expected’ sinking depth (= sinking speed  $\times$  time  
 491 since release). Blue (red) grid cells indicate that the median depth of particles in this cell is  
 492 deeper (shallower) than expected, based on a 1D gravitational model where  $z = w_s$ . [right] (d)  
 493 Probability Distribution Function (PDF) of particles as a function of depth for each velocity  
 494 class. The winter distribution is shown as thick lines, while the summer distribution is repre-  
 495 sented by the shaded regions. Triangle markers indicate the expected depth of particles after 25  
 496 days based on the 1D gravitational model, which is used as a reference to compute the depth  
 497 anomalies. Release depth is indicated by the thick dashed line.

498 In the winter, however, PDFs of particle density versus depth is wider, in agree-  
 499 ment with the stronger vertical ocean currents occurring in the winter (see Figure 5).  
 500 A top-view of the deviation in the downward particle flux from the traditionally con-

sidered 1D gravitational model can be seen in Figure 6 (panels (a)-(c)). Slower-sinking particles deviate more than faster-sinking particles, exhibiting median depth anomalies up to 50 m. This is due to the fact that slower-sinking particles spend more time in the mixed layer, where most of the stronger vertical currents tend to occur (Figure 5). An interesting result emerges from the spatial distribution of the depth-anomaly: both positive (i.e., particles are shallower than expected) and negative (i.e., particles are deeper than expected) anomalies are organized into features with a length-scale  $\mathcal{O}(1\text{-}10 \text{ km})$ . This further highlights the importance of winter submesoscale circulation for vertical fluxes of particles.

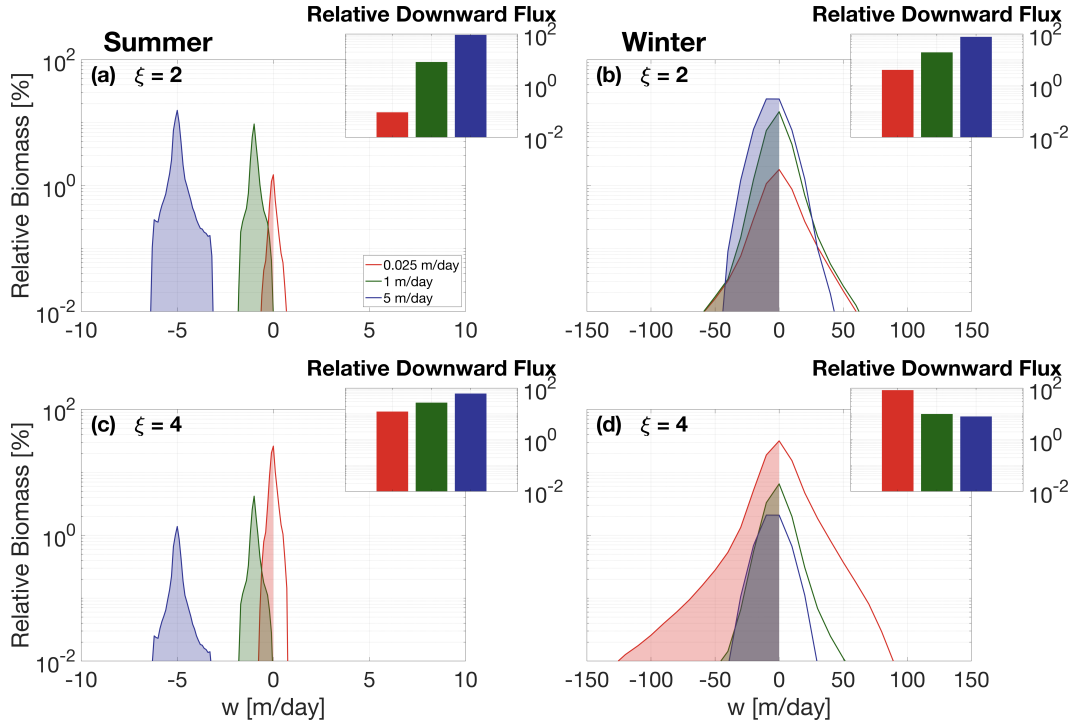
A relative amount of biomass is associated to the particles using Equation (8). PDFs of relative biomass as a function of the vertical velocity is shown in Figure 7. Following the traditional paradigm derived from the simple 1D gravitational model, the downward flux of biomass in the summer is dominated by faster-sinking particle classes capable of carrying particulate material downwards more efficiently. The contribution of slower-sinking particles, however, depends critically on the slope of the size spectrum (see Figure 4). As the Junge slope increases, the spectrum of biomass steepens, and the relative contribution of slower-sinking particles to the downward biomass flux significantly increases (Figure 7c). In fact, the contribution of slower-sinking particles to the summer downward flux increases by a factor 100 (from 0.1% to 10%) when the Junge slope varies from  $\xi = 2$  to  $\xi = 4$ . While significant, the impact of a change in the Junge slope in summer conditions does not challenge the dominant role played by faster-sinking particles. This result can be explained by the fact that, in the summer, vertical velocities are weak and vertical biomass fluxes are therefore gravitationally-driven ( $\langle w_s B \rangle > \langle w B \rangle$ ).

In the winter, PDFs of relative biomass as a function of vertical velocities present a much larger spread, with velocity magnitudes exceeding 50 m/day. For  $\xi = 2$ , the relative contribution of slower-sinking particles to the downward flux significantly increases from 0.1% in the summer to about 4% in the winter, demonstrating the impact advective velocities alone can have on vertical fluxes (Figure 7b). Nevertheless, slower-sinking particles remain a relatively small contributor to the total downward flux of biomass. When winter ocean dynamics are coupled with a steeper Junge slope, however, slower-sinking particles largely dominate the downward biomass flux. In our winter simulations with  $\xi = 4$ , we find that the slowest-sinking particle class is responsible for about 80% of the biomass flux (Figure 7d).

Our results show that both a steepening of the particle size spectrum and the presence of submesoscale dynamics can enhance the contribution of slower-sinking particles to the downward biomass flux. While the former is simply due to an increase in particle density in slower-sinking particle classes, the latter is attributed to the larger vertical velocity generated by submesoscale instabilities. When both are combined, as expected in the wintertime, slower-sinking particles then become the leading contributor to the downward biomass transport. However, slower-sinking particles are generally expected to remineralize on timescales shorter than their export timescale, fueling the argument that the focus should be upon faster-sinking particle classes. The impacts of remineralization on export are thus considered in the following section to test the robustness of the findings.

### 551 3.3 Particle Remineralization

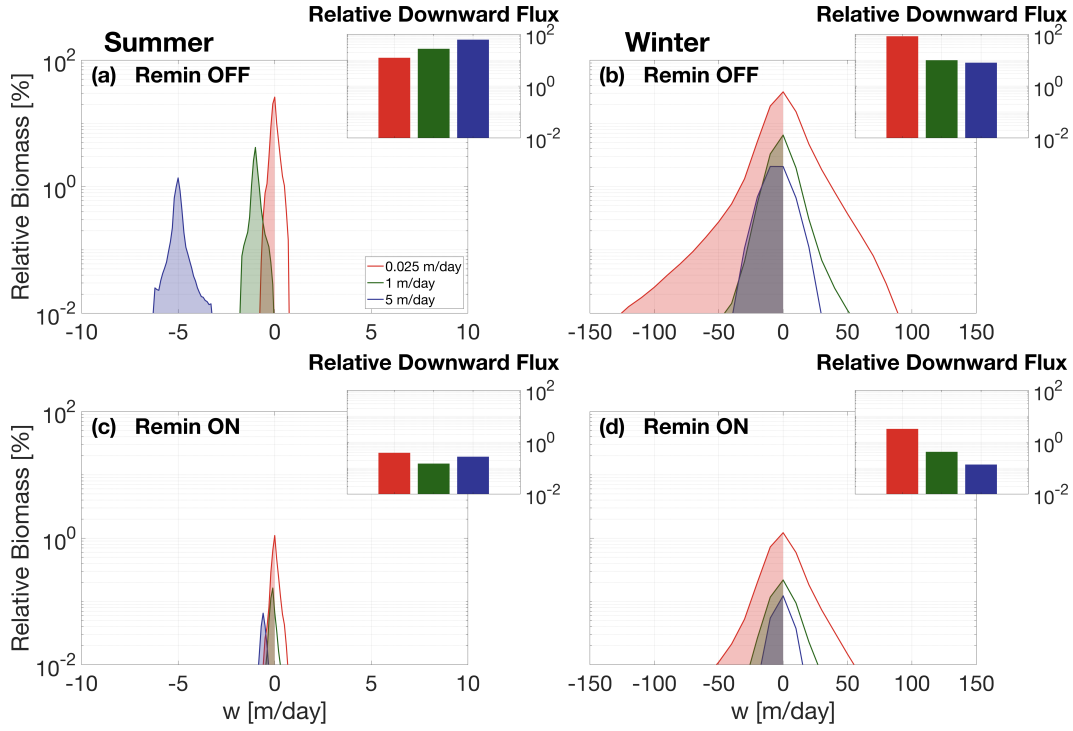
552 Both submesoscale dynamics and the Junge slope were identified as key factors  
 553 impacting the respective role played by different particle classes in driving downward  
 554 biomass fluxes. Simple Lagrangian particles were used to isolate the effects of these  
 555 two factors. In reality, however, sinking velocities of particulate matter varies in time  
 556 as the particles slowly remineralize. A remineralizing behavior was therefore imple-



525 **Figure 7.** Probability Distribution Function (PDF) of relative biomass versus vertical velocity  
 526 along particle trajectories in the summer case [left] and winter case [right], with a Junge slope  
 527 of 2 [top] and 4 [bottom]. Inserts show the integrated relative downward biomass flux associated  
 528 with each sinking-velocity class. Both winter dynamics and steeper Junge slopes tend to increase  
 529 the relative contribution of slower-sinking particles.

557 mented for the Lagrangian particles, using Equation (10), to investigate the impact  
 558 that remineralization processes have on our findings. The traditional paradigm relies  
 559 on the fact that slow-sinking particles tend to fully remineralize over short timescales,  
 560 further enhancing the importance of faster-sinking particles classes in driving down-  
 561 ward biomass fluxes. While this paradigm holds for flatter Junge slope, where the  
 562 biomass content is dominated by faster-sinking particles, it becomes unfit at steeper  
 563 slopes.

570 Figure 8 compares the relative biomass and downward biomass fluxes associated  
 571 with each of the modeled particle classes for  $\xi = 4$  with and without the remineral-  
 572 ization scheme. As previously detailed, downward fluxes of biomass are dominated  
 573 by faster-sinking particles during summertime and in the absence of remineralization.  
 574 This is due to the fact that the flux of biomass  $\langle w_{tot}B \rangle = \langle w_s B \rangle + \langle w B \rangle$  is driven by  
 575  $\langle w_s B \rangle$ , despite a smaller relative biomass content per particle. This is characteristic  
 576 of a gravitationally-driven system, where settling velocity dictates the contribution to  
 577 downward fluxes. Implementing remineralization processes, however, directly affects  
 578 the particle settling velocity which slows down as particles remineralize. This effect  
 579 can be seen in Figure 8c, where PDFs of relative biomass per particle class are shifted  
 580 towards weaker vertical velocities than in the absence of remineralization, as predicted  
 581 by Equation (10). As a result, the gravitationally-driven term  $\langle w_s B \rangle$  decreases with  
 582 time, and the downward flux of biomass becomes generally advectively-driven by day 25  
 583 (Figure 8). In an advectively-driven system where  $\langle w_s B \rangle < \langle w B \rangle$ , the relative amount of  
 584 biomass content in a particle class becomes important and dictates the respective con-  
 585 tribution of each particle class to the total downward biomass fluxes. This shift from a



564 **Figure 8.** Probability Distribution Function (PDF) of relative biomass versus vertical ve-  
 565 locity along particle trajectories in the summer case [left] and winter case [right], ignoring [top]  
 566 and including [bottom] particle remineralization, for  $\xi = 4$  and 25 days after particle release.  
 567 Inserts show the integrated relative downward biomass flux associated with each sinking-velocity  
 568 class. Remineralization processes have the greatest impact on fast-sinking particles, especially in  
 569 summer dynamics.

586 gravitationally-driven to an advectively-driven system is observed when implementing  
 587 particle remineralization in the summer (Figure 8c): in the absence of remineralization,  
 588 faster-sinking particles dominate the downward biomass fluxes (60%; see Figure 8a).  
 589 When remineralization processes are considered, slower-sinking particles become the  
 590 dominant contributor to biomass fluxes (see inset in Figure 8c). As shown in Figure  
 591 7, downward biomass fluxes in the wintertime are generally advectively-driven, due  
 592 to the larger vertical velocities associated with wintertime ocean dynamics. Biomass  
 593 fluxes are dominated by the slower-sinking particles, representing 82% of the down-  
 594 ward biomass flux (Figure 8b). Even after implementing our remineralization scheme,  
 595 slower-sinking particles remain the largest contributor to downward biomass fluxes  
 596 (87%; see Figure 8d).

597 These results highlight the importance in considering slower-sinking particle  
 598 classes when considering downward biomass fluxes. It also demonstrates that, con-  
 599 trarily to the traditional paradigm, remineralization processes enhance the role played  
 600 by slower-sinking particles in biomass fluxes, in cases where the biomass spectrum  
 601 slope is negative.

602 The timescales over which the system transitioned from an gravitationally-driven  
 603 to an advectively-driven system depends on the remineralization model used.

604 **4 Discussion**605 **4.1 Dynamical Regimes**

606 *Papa-summer* and *Papa-winter* experiments were designed to statistically cap-  
 607 ture the ocean dynamics at Station Papa (145°W, 50°N) in the Northeast Pacific  
 608 Ocean. After spin-up, the model demonstrated similar distributions of both horizontal  
 609 ( $M^2$ ) and vertical ( $N^2$ ) density gradients to observational estimates from underwater  
 610 gliders (see Figures 2, 3, and 5). The two experiments, however, show significantly  
 611 different distributions of  $M^2$ , with the winter distribution exhibiting a longer tail, due  
 612 to sharper density gradients. The tail of the wintertime distribution is only partially  
 613 captured by the glider data, due to the fact that underwater gliders sampled gradients  
 614 at spatial scales of 10 km and greater, while the model has a horizontal resolution of  
 615 500 m, allowing sharper submesoscale fronts and filaments to be formed.

616 Studies investigating submesoscale dynamics traditionally focused on regions  
 617 where the presence of submesoscale fronts and filaments are established, such as west-  
 618 ern boundary currents with strong gradients (D'Asaro, Lee, Rainville, Harcourt, &  
 619 Thomas, 2011; Thomas, Taylor, Ferrari, & Joyce, 2013), or the edge of mesoscale fea-  
 620 tures (van Haren et al., 2006; Waite et al., 2016). The seasonality in submesoscale  
 621 dynamics captured in the glider dataset at Station Papa and reflected in the model  
 622 experiments, echoes the behavior seen from recent observational studies conducted  
 623 at a similar latitude in the Atlantic Ocean, which demonstrate the intensification of  
 624 submesoscale dynamics in the wintertime (Buckingham et al., 2016; Thompson et al.,  
 625 2016). Despite being sometimes qualified as an “eddy desert” with low kinetic energy  
 626 (Chelton, Schlax, & Samelson, 2011), ocean characteristics in the eastern part of the  
 627 Pacific subpolar gyre suggest the presence of submesoscale features in the wintertime:  
 628 strong density gradients, localized Rossby numbers of order 1, a balanced Richardson  
 629 number  $Rib = \frac{f^2 N^2}{M^4}$  smaller than 1, a positively skewed distribution in vorticity, and a  
 630 negatively skewed distribution of vertical velocities (see Figure 5; Buckingham et al.,  
 631 2016; Rudnick, 2001; Thomas, Tandon, & Mahadevan, 2013).

632 Strong downward velocities are hypothesized to enhance POC export by advect-  
 633 ing slower-sinking particles out of the mixed layer. *Papa-winter* indeed exhibits vertical  
 634 velocities more than 20 times larger than in *Papa-summer*. The vertical currents in  
 635 *Papa-winter*, however, tend to be much patchier than the weaker vertical currents  
 636 observed in *Papa-summer*. Because both particle production and downward vertical  
 637 velocities present a high degree of patchiness, it requires a certain level of covariance  
 638 between the two fields for the export to effectively be enhanced (Mahadevan et al.,  
 639 2012). A more realistic seeding strategy for Lagrangian particles, such as one guided  
 640 by biological tracers, would likely provide important information towards a better  
 641 understanding of the effects of patchiness on POC export at submeso-scales

642 The hypothesis tested in this study is that submesoscale activity enhances export  
 643 of particulate matter at Station Papa by shortening the export timescale of particulate  
 644 matter. The wintertime intensification in submesoscale activity has the potential to  
 645 indeed enhance export (see discussion in Section 4.2). However, the seasonal cycle  
 646 in submesoscale activity is out of phase with the one in net community productivity,  
 647 which peaks in the spring and summertime when the mixed layer is shallower (Plant  
 648 et al., 2016). Two mechanisms are therefore present to potentially sustain a year-long  
 649 POC export flux: In the winter, less particulate material is present in the mixed layer,  
 650 but active submesoscale dynamics tend to enhance the POC export flux by advecting  
 651 the more numerous slower-sinking particles into the ocean interior. In the summer,  
 652 the production of POC is at its yearly maximum, but export tends to be dominated  
 653 by gravitational sinking, which favors faster-sinking particles and thus exclude part of  
 654 the particle spectrum from contributing to the export flux.

## 655      4.2 Downward Fluxes

656      Analyses of particle tracking experiments reveal that the contribution of slower-  
 657      sinking particles to the downward particulate flux depends on two main factors: (1)  
 658      the dynamics of the oceanic flow field, and (2) the slope of the size spectrum (i.e., the  
 659      Junge slope  $\xi$ ).

660      Mixed layer ocean dynamics at station Papa change significantly between the  
 661      winter and the summer. In the winter, submesoscale dynamics are intensified, and  
 662      sharp fronts and filaments develop in the mixed layer. This seasonal change in dy-  
 663      namics is consistent with recent observations (Buckingham et al., 2016; Thompson  
 664      et al., 2016), and models (Brannigan, Marshall, Naveira-Garabato, & George Nurser,  
 665      2015; Callies et al., 2015; Rocha, Gille, Chereskin, & Menemenlis, 2016) characterizing  
 666      the seasonal cycle of submesoscale dynamics. The winter intensification in subme-  
 667      soscale dynamics was proven to have an important impact on the downward flux of all  
 668      sinking-velocity classes modeled in this experiment.

669      In the summer, gravitational sinking governs a downward particulate flux, which  
 670      is dominated by faster-sinking particles, with little to no contribution from slower-  
 671      sinking particles. In the winter, however, vertical fluxes tend to be advectively-driven,  
 672      which leads to a slightly weaker downward flux of faster-sinking particles than in the  
 673      summer due to resuspension, but a much larger flux of slower-sinking particles, which  
 674      are present in far greater numbers (Figure 7). The gravitationally-driven flux in the  
 675      summer is mechanistically different from the advectively-driven winter flux, which  
 676      raises the question as to which process is most efficient in driving a downward flux of  
 677      particulate material.

678      In the absence of remineralization, both a steeper size spectrum slope ( $\xi > 3$  in  
 679      this case) and enhanced submesoscale dynamics, increase the contribution of slower-  
 680      sinking particle classes to the downward biomass flux. This is only when both of  
 681      these conditions are combined, however, that slower-sinking particles dominate the  
 682      downward flux of biomass (Figure 7). This is a significant result, as Junge slopes  
 683      greater than 3 have been observed in the ocean (Kostadinov, Siegel, & Maritorena,  
 684      2009; White et al., 2015). The threshold value of  $\xi = 3$  for a change in the biomass  
 685      spectral slope (see Figure 4b) is of course a consequence of first-order approximations  
 686      used in this study describing the relationships between particle size, sinking veloc-  
 687      ity, and biomass content. Nevertheless, our results demonstrate the importance of  
 688      including the smaller particle size range of the particle spectrum, in the estimation or  
 689      measurement of vertical fluxes, especially when submesoscale dynamics are active. It  
 690      also highlights the importance of better constraining the relationships linking particle  
 691      size, sinking velocity, and biomass content.

692      Introducing remineralization processes significantly decreases the biomass flux.  
 693      Counter-intuitively, however, the implementation of a remineralization scheme further  
 694      strengthens the contribution of slower-sinking particles to the biomass flux (Figure  
 695      8). This can be explained by the fact that remineralization processes have a greater  
 696      impact on sinking-velocity classes that rely on gravitational sinking to be exported, as  
 697      these particles decelerate as they remineralize. In the summer, all particle classes are  
 698      similarly affected by remineralization, as downward fluxes are gravitationally-driven.  
 699      In the winter, however, slower-sinking particles are exported through advective pro-  
 700      cesses. Their export timescale is barely affected by remineralization processes as it  
 701      only depends on local ocean dynamics.

702      The results of this study suggest that slow- and non-sinking particles must be  
 703      considered when studying the downward flux of particulate matter in the upper ocean.  
 704      The patchiness associated with both particle production and submesoscale features  
 705      poses a real observational challenge to properly resolve vertical fluxes. Based on our

706 findings, subsequent studies should focus on testing the impact of patchiness on vertical  
 707 fluxes. In the wintertime, when size spectral slope is steep and submesoscale dynamics  
 708 most active, vertical fluxes could be grossly underestimated depending on the level of  
 709 co-occurrence between particle production and stronger vertical currents.

## 710 5 Conclusion

711 The main conclusions of this study are:

- 712 1. Ocean dynamics in the subpolar Northeast Pacific exhibit a seasonal cycle with  
     713 low submesoscale activity in the summertime, and more submesoscale features  
     714 present in the wintertime. Submesoscale dynamics generate larger, and asym-  
     715 metric, vertical currents leading to a vertical biomass flux driven by advective  
     716 processes, as opposed to gravitational sinking in the summertime.
- 717 2. Submesoscale dynamics generally enhance the downward particulate flux by  
     718 increasing the contribution of slower-sinking particles to the total flux through  
     719 advective transport. The slower-sinking particles are found to be significant  
     720 for export, and can be even make the dominant contribution under certain  
     721 conditions.
- 722 3. The contribution of slower-sinking particles to the downward biomass flux de-  
     723 pends on the slope of the particle size spectra (i.e., the Junge Slope), that  
     724 controls the relative number of particles per size class. Two cases emerge from  
     725 this study:
  - 726 (a) If the Junge slope is smaller than 3, larger particles contribute most to vertical  
     727 biomass fluxes independently of flow dynamics, as there are no mechanisms  
     728 capable of selectively advecting slower-sinking particles. The system is de-  
     729 scribed as gravitationally-driven.
  - 730 (b) If the Junge slope is greater than 3, as most commonly observed, ocean  
     731 dynamics become key for determining which particle classes dominate the  
     732 downward flux. As submesoscale dynamics become more active, ageostrophic  
     733 circulations leading to larger vertical velocities develop. In these conditions,  
     734 downward biomass fluxes are largely driven by the slower-sinking particle  
     735 classes.
- 736 4. Remineralization processes logically reduce the amount of biomass flux. How-  
     737 ever, it unexpectedly enhances the role of slower-sinking particles, which are are  
     738 advectively transported. The impact of remineralization is greater on faster-  
     739 sinking particles since it affects both the biomass content and their sinking  
     740 velocity.

## 741 Acknowledgments

742 The work was funded by NASA grant NNX16AR48G, to complement the EX-  
 743 port Processes in the global Ocean from RemoTe Sensing (EXPORTS) program. We  
 744 would like to thank A. Thompson (Caltech) for his useful comments and suggestions,  
 745 N. Pelland (NOAA) and Charlie Eriksen (University of Washington) for sharing the  
 746 glider data collected at Ocean Station Papa, as well as Sebastian Essink for his assis-  
 747 tance in developing the particle-tracking code. All data used in this manuscript are  
 748 publicly available: Ocean Station Papa data is available on PMEL's website ([https://www.pmel.noaa.gov/ocs/Papa/](https://www.pmel.noaa.gov/ocs/Papa;); ?) and gridded Argo products can be downloaded at  
 749 <http://www.seanoe.org/data/00348/45945> (?). Glider data is archived at the Uni-  
 750 versity of Washington's Library ([https://digital.lib.washington.edu/researchworks/](https://digital.lib.washington.edu/researchworks/handle/1773/41656)  
 751 [handle/1773/41656](https://digital.lib.washington.edu/researchworks/handle/1773/41656); ?).

753 **References**

- Bach, L. T., Riebesell, U., Sett, S., Febiri, S., Rzepka, P., & Schulz, K. G. (2012). An approach for particle sinking velocity measurements in the 3400  $\mu\text{m}$  size range and considerations on the effect of temperature on sinking rates. *Marine Biology*, 159(8), 1853–1864. doi: 10.1007/s00227-012-1945-2
- Bower, A. S., & Rossby, T. (1989). Evidence of Cross-Frontal Exchange Processes in the Gulf Stream Based on Isopycnal RAFOS Float Data. *Journal of Physical Oceanography*, 19(9), 1177–1190. doi: 10.1175/1520-0485(1989)019<1177:EOCFEP>2.0.CO;2
- Brannigan, L., Marshall, D. P., Naveira-Garabato, A., & George Nurser, A. (2015). The seasonal cycle of submesoscale flows. *Ocean Modelling*, 92, 69–84. doi: 10.1016/j.ocemod.2015.05.002
- Buckingham, C. E., Naveira Garabato, A. C., Thompson, A. F., Brannigan, L., Lazar, A., Marshall, D. P., ... Belcher, S. E. (2016). Seasonality of submesoscale flows in the ocean surface boundary layer. *Geophysical Research Letters*, 43(5), 2118–2126. doi: 10.1002/2016GL068009
- Callies, J., Ferrari, R., Klymak, J. M., & Gula, J. (2015). Seasonality in submesoscale turbulence. *Nature communications*, 6, 6862. doi: 10.1038/ncomms7862
- Chelton, D. B., Schlax, M. G., & Samelson, R. M. (2011). Global observations of nonlinear mesoscale eddies. *Progress in Oceanography*, 91(2), 167–216. doi: 10.1016/j.pocean.2011.01.002
- D'Asaro, E., Lee, C., Rainville, L., Harcourt, R., & Thomas, L. (2011). Enhanced Turbulence and Energy Dissipation at Ocean Fronts. *Science*, 332(6027), 318–322. doi: 10.1126/science.1201515
- Döös, K., Kjellsson, J., & Jönsson, B. (2013). TRACMASS – A Lagrangian Trajectory Model. In *Preventive methods for coastal protection* (pp. 225–249). Heidelberg: Springer International Publishing. doi: 10.1007/978-3-319-00440-2\_7
- Estapa, M. L., Siegel, D. A., Buesseler, K. O., Stanley, R. H. R., Lomas, M. W., & Nelson, N. B. (2015). Decoupling of net community and export production on submesoscales in the Sargasso Sea. *Global Biogeochemical Cycles*, 29(8), 1266–1282. doi: 10.1002/2014GB004913
- Falkowski, P. G., Barber, R. T., & Smetacek, V. (1998). Biogeochemical Controls and Feedbacks on Ocean Primary Production. *Science*, 281(5374), 200–206. doi: 10.1126/science.281.5374.200
- Fox-Kemper, B., Ferrari, R., & Hallberg, R. (2008). Parameterization of Mixed Layer Eddies. Part I: Theory and Diagnosis. *Journal of Physical Oceanography*, 38(6), 1145–1165. doi: 10.1175/2007JPO3792.1
- Gaillard, F., Autret, E., Thierry, V., Galaup, P., Coatanoan, C., & Loubrieu, T. (2009). Quality Control of Large Argo Datasets. *Journal of Atmospheric and Oceanic Technology*, 26(2), 337–351. Retrieved from <https://doi.org/10.1175/2008JTECH0552.1> doi: 10.1175/2008JTECHO552.1
- Gaillard, F., Reynaud, T., Thierry, V., Kolodziejczyk, N., & von Schuckmann, K. (2016). In situ-based reanalysis of the global ocean temperature and salinity with isas: Variability of the heat content and steric height. *Journal of Climate*, 29(4), 1305–1323. doi: 10.1175/JCLI-D-15-0028.1
- Harrison, P. J., Whitney, F. A., Tsuda, A., Saito, H., & Tadokoro, K. (2004). Nutrient and Plankton Dynamics in the NE and NW Gyres of the Subarctic Pacific Ocean. *Journal of Oceanography*, 60(1), 93–117. doi: 10.1023/B:JOCE.0000038321.57391.2a
- Hoskins, B. J., & Bretherton, F. P. (1972). Atmospheric Frontogenesis Models: Mathematical Formulation and Solution. *Journal of the Atmospheric Sciences*, 29(1), 11–37. doi: 10.1175/1520-0469(1972)029<0011:AFMMFA>2.0.CO;2
- Iversen, M. H., & Ploug, H. (2010). Ballast minerals and the sinking carbon flux in the ocean: carbon-specific respiration rates and sinking velocity of marine snow

- 808 aggregates. *Biogeosciences*, 7(9), 2613–2624. doi: 10.5194/bg-7-2613-2010
- 809 Iversen, M. H., & Ploug, H. (2013). Temperature effects on carbon-specific respi-  
810 ration rate and sinking velocity of diatom aggregates - potential implications  
811 for deep ocean export processes. *Biogeosciences*, 10(6), 4073–4085. doi:  
812 10.5194/bg-10-4073-2013
- 813 Klein, P., & Lapeyre, G. (2009). The Oceanic Vertical Pump Induced by Mesoscale  
814 and Submesoscale Turbulence. *Annual Review of Marine Science*, 1(1), 351–  
815 375. doi: 10.1146/annurev.marine.010908.163704
- 816 Kostadinov, T. S., Siegel, D. A., & Maritorena, S. (2009). Retrieval of the particle  
817 size distribution from satellite ocean color observations. *Journal of Geophysical  
818 Research*, 114(C9), C09015. doi: 10.1029/2009JC005303
- 819 Lévy, M., Ferrari, R., Franks, P. J. S., Martin, A. P., & Rivière, P. (2012). Bringing  
820 physics to life at the submesoscale. *Geophysical Research Letters*, 39(14), n/a–  
821 n/a. doi: 10.1029/2012GL052756
- 822 Lévy, M., Mémery, L., & Madec, G. (1998). The onset of a bloom after deep winter  
823 convection in the northwestern Mediterranean sea: mesoscale process study  
824 with a primitive equation model. *Journal of Marine Systems*, 16(1-2), 7–21.  
825 doi: 10.1016/S0924-7963(97)00097-3
- 826 Mahadevan, A. (2016). The Impact of Submesoscale Physics on Primary Produc-  
827 tivity of Plankton. *Annual Review of Marine Science*, 8(1), 161–184. doi: 10  
828 .1146/annurev-marine-010814-015912
- 829 Mahadevan, A., D'Asaro, E., Lee, C., & Perry, M. J. (2012). Eddy-Driven Strat-  
830 ification Initiates North Atlantic Spring Phytoplankton Blooms. *Science*,  
831 337(6090), 54–58. doi: 10.1126/science.1218740
- 832 Mahadevan, A., Oliger, J., & Street, R. (1996a). A Nonhydrostatic Mesoscale Ocean  
833 Model. Part II: Numerical Implementation. *Journal of Physical Oceanog-  
834 raphy*, 26(9), 1881–1900. Retrieved from [http://journals.ametsoc.org/doi/abs/10.1175/1520-0485\(1996\)026%3C1881:ANMOMP%3E2.0.CO;2](http://journals.ametsoc.org/doi/abs/10.1175/1520-0485(1996)026%3C1881:ANMOMP%3E2.0.CO;2)  
835 .CO;2[http://journals.ametsoc.org/doi/abs/10.1175/1520-0485\(1996\)026%3C1881%3AANMOMP%3E2.0.CO%3B2](http://journals.ametsoc.org/doi/abs/10.1175/1520-0485(1996)026%3C1881%3AANMOMP%3E2.0.CO%3B2) doi:  
836 10.1175/1520-0485(1996)026(1881:ANMOMP)2.0.CO;2  
837  
838 Mahadevan, A., Oliger, J., & Street, R. (1996b). A Nonhydrostatic mesoscale ocean  
839 model. Part I: Well-posedness and scaling. *Journal of Physical Oceanography*,  
840 26(9), 1868–1880. doi: 10.1175/1520-0485(1996)026<1868:ANMOMP>2.0.CO;  
841 2  
842 Mahadevan, A., & Tandon, A. (2006). An analysis of mechanisms for submesoscale  
843 vertical motion at ocean fronts. *Ocean Modelling*, 14(3-4), 241–256. doi: 10  
844 .1016/J.OCEMOD.2006.05.006
- 845 McDonnell, A. M. P., & Buesseler, K. O. (2010). Variability in the average sinking  
846 velocity of marine particles. *Limnology and Oceanography*, 55(5), 2085–2096.  
847 doi: 10.4319/lo.2010.55.5.2085
- 848 McWilliams, J. C. (2016). Submesoscale currents in the ocean. *Proceedings of the  
849 Royal Society A: Mathematical, Physical and Engineering Science*, 472(2189).
- 850 Mensa, J. A., Garraffo, Z., Griffa, A., Özgökmen, T. M., Haza, A., & Veneziani, M.  
851 (2013). Seasonality of the submesoscale dynamics in the Gulf Stream region.  
852 *Ocean Dynamics*, 63(8), 923–941. doi: 10.1007/s10236-013-0633-1
- 853 Mesinger, F., DiMego, G., Kalnay, E., Mitchell, K., Shafran, P. C., Ebisuzaki, W.,  
854 ... Shi, W. (2006). North american regional reanalysis. *Bulletin of the Ameri-  
855 can Meteorological Society*, 87(3), 343-360. doi: 10.1175/BAMS-87-3-343
- 856 Omand, M. M., D'Asaro, E. A., Lee, C. M., Perry, M. J., Briggs, N., Cetini, I.,  
857 & Mahadevan, A. (2015). Eddy-driven subduction exports particulate or-  
858 ganic carbon from the spring bloom. *Science*, 348(6231), 222–225. doi:  
859 10.1126/science.1260062
- 860 Pelland, N. A., Eriksen, C. C., & Cronin, M. F. (2016). Seaglider surveys at Ocean  
861 Station Papa: Circulation and watermass properties in a meander of the North

- 863 Pacific Current. *Journal of Geophysical Research: Oceans*, 121, 6816–6846.  
864 doi: 10.1002/2016JC011920
- 865 Plant, J. N., Johnson, K. S., Sakamoto, C. M., Jannasch, H. W., Coletti, L. J.,  
866 Riser, S. C., & Swift, D. D. (2016). Net community production at Ocean Sta-  
867 tion Papa observed with nitrate and oxygen sensors on profiling floats. *Global  
868 Biogeochemical Cycles*, 30(6), 859–879. doi: 10.1002/2015GB005349
- 869 Ploug, H., Iversen, M. H., Koski, M., & Buitenhuis, E. T. (2008). Production,  
870 oxygen respiration rates, and sinking velocity of copepod fecal pellets: Direct  
871 measurements of ballasting by opal and calcite. *Limnology and Oceanography*,  
872 53(2), 469–476. doi: 10.4319/lo.2008.53.2.0469
- 873 Rocha, C. B., Gille, S. T., Chereskin, T. K., & Menemenlis, D. (2016, nov). Season-  
874 ality of submesoscale dynamics in the Kuroshio Extension. , 43(21), 11,304–  
875 11,311. doi: 10.1002/2016GL071349
- 876 Rudnick, D. L. (2001). On the skewness of vorticity in the upper ocean. *Geophysical  
877 Research Letters*, 28(10), 2045–2048. doi: 10.1029/2000GL012265
- 878 Sherry, N. D., Boyd, P. W., Sugimoto, K., & Harrison, P. J. (1999). Seasonal and  
879 spatial patterns of heterotrophic bacterial production, respiration, and biomass  
880 in the subarctic NE Pacific. *Deep-Sea Research Part II: Topical Studies in  
881 Oceanography*, 46(11-12), 2557–2578. doi: 10.1016/S0967-0645(99)00076-4
- 882 Thomas, L. N., Tandon, A., & Mahadevan, A. (2013). Submesoscale processes and  
883 dynamics. In *Ocean modeling in an eddying regime* (p. 17-38). American Geo-  
884 physical Union (AGU). doi: 10.1029/177GM04
- 885 Thomas, L. N., Taylor, J. R., Ferrari, R., & Joyce, T. M. (2013). Symmetric in-  
886 stability in the Gulf Stream. *Deep Sea Research Part II: Topical Studies in  
887 Oceanography*, 91, 96–110. doi: 10.1016/j.dsr2.2013.02.025
- 888 Thompson, A. F., Lazar, A., Buckingham, C., Naveira Garabato, A. C., Damerell,  
889 G. M., & Heywood, K. J. (2016). Open-Ocean Submesoscale Motions: A Full  
890 Seasonal Cycle of Mixed Layer Instabilities from Gliders. *Journal of Physical  
891 Oceanography*, 46(4), 1285–1307. doi: 10.1175/JPO-D-15-0170.1
- 892 van Haren, H., Millot, C., & Taupier-Letage, I. (2006). Fast deep sinking in Medi-  
893 teranean eddies. *Geophysical Research Letters*, 33(4), L04606. doi: 10.1029/  
894 2005GL025367
- 895 Waite, A. M., Stemmann, L., Guidi, L., Calil, P. H. R., Hogg, A. M. C., Feng, M.,  
896 ... Gorsky, G. (2016). The wineglass effect shapes particle export to the deep  
897 ocean in mesoscale eddies. *Geophysical Research Letters*, 43(18), 9791–9800.  
898 doi: 10.1002/2015GL066463
- 899 White, A. E., Letelier, R. M., Whitmire, A. L., Barone, B., Bidigare, R. R., Church,  
900 M. J., & Karl, D. M. (2015). Phenology of particle size distributions  
901 and primary productivity in the North Pacific subtropical gyre (Station  
902 ALOHA). *Journal of Geophysical Research: Oceans*, 120(11), 7381–7399.  
903 doi: 10.1002/2015JC010897